

Annual Review of Physical Chemistry

Chirality-Induced Spin Selectivity in Hybrid Organic-Inorganic Perovskite Semiconductors

Yifan Dong, Matthew P. Hautzinger, Md Azimul Haque, and Matthew C. Beard

National Renewable Energy Laboratory, Golden, Colorado, USA; email: yifan.dong@nrel.gov, matthew.hautzinger@nrel.gov, mdazimul.haque@nrel.gov, matt.beard@nrel.gov

Annu. Rev. Phys. Chem. 2025. 76:519–37

First published as a Review in Advance on February 14, 2025

The *Annual Review of Physical Chemistry* is online at physchem.annualreviews.org

<https://doi.org/10.1146/annurev-physchem-082423-032933>

Copyright © 2025 by the author(s). This work is licensed under a Creative Commons Attribution 4.0 International License, which permits unrestricted use, distribution, and reproduction in any medium, provided the original author and source are credited. See credit lines of images or other third-party material in this article for license information.



ANNUAL
REVIEWS **CONNECT**

www.annualreviews.org

- Download figures
- Navigate cited references
- Keyword search
- Explore related articles
- Share via email or social media

Keywords

chirality-induced spin selectivity, spin-to-charge conversion, spin polarization, circularly polarized light, chirality, chiral crystals, chiral axis, organic-inorganic hybrid semiconductors, asymmetry, chiral halide perovskite

Abstract

The movement of charges through a chiral medium results in a spin-polarized charge current. This phenomenon, known as the chirality-induced spin selectivity (CISS) effect, enables control over spin populations without the need for magnetic components and operates at room temperature. CISS has been discovered in a range of chiral media and most prominently studied in chiral organic molecular species. Chiral hybrid organic-inorganic perovskite semiconductors combine the unique and functional aspects of inorganic semiconductors with chiral molecules. The inorganic component borrows the homochirality of the organic component to yield a unique family of highly tunable chiral semiconductors, where the enantiomeric purity is defined by the organic component. Semiconductors already form the backbone of modern-day technologies. Adding chirality and control over spin through CISS provides new avenues for creative technological development. This review is intended to be an introduction to these unique systems and the demonstrations of CISS and spin control.

1. INTRODUCTION

Chirality-induced spin selectivity (CISS) refers to when the electron spin orientation is determined by the chirality of the transport medium. In 1999, David Waldeck, Ron Naaman, and colleagues (1) observed preferential scattering of polarized electrons when they passed through oriented chiral molecules. Since then, a variety of observations have demonstrated that the spin orientation of electrons is intimately tied to the chirality of the molecular framework. A few years ago, we observed that CISS can also occur in oriented hybrid organic-inorganic perovskite semiconductors (HOIS) when the organic component, fixed within the hybrid crystal structure, consists of small chiral ammonium cations (2, 3). These hybrid systems have beneficial properties not found in purely chiral organic systems and are absent in purely inorganic semiconductors. The enantiomeric purity is defined by the chiral organic cation type while the electronic properties are defined by the inorganic components. In this article, we discuss the pertinent aspects of this new class of chiral semiconductors that can both take advantage of the CISS effect for optoelectronic applications and exhibit tunable aspects that can be exploited to better understand and ultimately control the connection between structural chirality and CISS. We discuss recent measurements of CISS in chiral hybrid organic-inorganic perovskite semiconductors (c-HOIS) and provide critical insight and suggested areas for further understanding and exploration of CISS in chiral perovskite semiconductors.

The family of c-HOIS that we are discussing here consists of a framework of metal halide polyhedra spaced by noncoordinating chiral A-site organic cations. The nonchiral version of these semiconductors is being actively pursued for solar cell and light-emitting applications because they exhibit extraordinary semiconducting properties, represented by the methylammonium, formamidinium, and cesium lead halide perovskite semiconductors (4). These hybrid semiconductors have a great deal of composition and structural tunability that can be harnessed for a variety of potential applications. Typically, the band edges consist of extended states from the metal and halide components with little influence from the organic subcomponents. However, the organic component dictates the dimensionality, structure, and motif of the inorganic components through sterics and hydrogen bonding, which determine the resulting extended electronic structure and related properties such as charge carrier mobilities, bandgap, exciton binding energy, optical absorption, and photoluminescence efficiency.

Defining characteristics of the HOIS are their high degree of crystallinity and, when cast as thin films, their textured self-assembly. Because the chiral molecules that make up the extended global crystalline structure lack a center of inversion, the resulting hybrid semiconductor also lacks a center of inversion and can exhibit properties that are only found in non-centrosymmetric crystal structures, such as bulk second harmonic generation (5, 6), bulk photovoltaic effect (7), ferroelectricity (8), circular dichroism (CD) (9), and circularly polarized photoluminescence (10). In this article, we mostly confine the discussion to the observation of CISS and the resulting control over spin populations in c-HOIS. Similarly, we are mostly interested in the ability of these chiral semiconductors to control spin populations/polarizations at room temperature. Combining the attributes and tunability of semiconductors with the ability to control spin populations under ambient conditions has been a goal for many years (11, 12). CISS in chiral hybrid semiconductors represents a new approach to this important physical chemistry challenge.

2. STRUCTURAL CHIRALITY

Structural chirality is defined by the lack of mirror and inversion symmetry. Inorganic materials, such as cinnabar (HgS), tellurium (Te), and α -quartz, have enantiomorphic pairs in the $P3_121$ or

$P3_221$ space groups with a 3_1 (3_2) screw axis inducing a helical chirality (13). This broken symmetry leads to interesting nonlinear and chiral optoelectronic properties, yet there is currently a lack of methods for producing homochiral inorganic materials. Organic molecules/compounds readily host point chirality due to the connectivity of sp^3 carbons. Enantioselective synthesis or chiral separations enable homochiral molecules and polymers. However, organics have limited electronic properties that can be enhanced with their chirality. Conductive chiral polymers are an interesting class of chiral organic semiconductors but typically lack long-range order.

HOIS benefit from the characteristics of both inorganic and organic properties. The inorganic metal halide framework displays extraordinary defect tolerance, coupled with large carrier diffusion lengths and absorption coefficients, resulting in excellent optoelectronic properties (14, 15). A wide variety of organic ammonium cations has been incorporated with metal halides, inducing the unique connectivity of the inorganic motifs and imparting unique properties on the resulting compounds (16, 17). This includes the incorporation of chiral organics with metal halides where the chiral organic component imparts chirality on to the structures (18). These hybrid compounds can easily be made homochiral with the choice of the chiral organic dictating the enantiomorph while maintaining the optoelectronic properties of the inorganic component.

The first c-HOIS structures reported were based on R/S- α -methylbenzylammonium (R/S-MBA) incorporated with PbX ($X = Cl, Br, \text{ and } I$) (19, 20). The c-HOIS structures largely follow the same trends as their achiral counterparts in that they form 2D, 1D, and 0D connectivity as previously described (16, 17) with the exception that the incorporation of chiral organics results in a further loss of symmetry; e.g., $(PEA)_2PbI_4$ (PEA is phenylethylammonium) crystallizes in the centrosymmetric $P1$ space group while replacing PEA with R/S-MBA results in the $P2_12_12_1$ space group (21). The chiral organic ammoniums themselves lack inversion and mirror plane symmetry, and incorporating them into the metal halides results in a global structure that fits into one of the 65 Sohncke space groups, that is, the class of space groups with only translational, rotational, and rototranslational symmetry. An interesting aspect of crystal structures of chiral organics is that an estimated 52% and 34% crystallize in the $P2_12_12_1$ and $P2_1$ space groups, respectively (22). While a much smaller sample size, a trend of the 2D c-HOIS is emerging that they too commonly fall into the $P2_12_12_1$ or $P2_1$ space groups (19, 23–32). This is reasonable as it is the chiral organic component imparting the chirality; the space group must incorporate the symmetry of the organic molecules that make up the global structure.

Here we discuss the symmetry and structure of 2D c-HOIS and the possible implications of this structure in further detail. A 2_1 (n_m) screw axis is a $1/2$ (m/n) unit cell translation followed by a 180° ($360^\circ/n$) rotation (**Figure 1a**). The $P2_12_12_1$ space group has a screw axis along each crystallographic direction, and the $P2_1$ space group has a screw axis only along one crystallographic direction. A common misperception of the 2_1 screw axis is that the mathematical definition of this symmetry operation is not inherently chiral in a simplified definition of chirality: an object that is distinguishable from its mirror image. Thus, the 2_1 screw axis itself does not have enantiomeric pairs. However, when atoms pack into these space groups, they must pack with a chiral asymmetric unit; that is, the smallest collection of atoms that can be symmetry adapted to produce the full unit cell is chiral. Without this chiral asymmetric unit, a higher-order symmetry operation can be used to describe the symmetry, as previously clarified in References 33 and 34. The chirality of this symmetry operation is best shown with an example: the 2D c-HOIS $(S\text{-NEA})_2PbBr_4$ (S-NEA is S-naphthylethylammonium), which fits in the $P2_1$ space group. When observing the lead octahedra, with uniquely bonded bromide atoms highlighted in different colors (i.e., unique crystallographic sites), one can see how the screw operation elicits chirality (**Figure 1b**). There is what can be described as a 3D screw, which cannot be superimposed with the mirror image of itself. An

Screw axis:

a symmetry operation written n_m , consisting of a translation of the distance m/n times the lattice vector, followed by a $360^\circ/n$ rotation

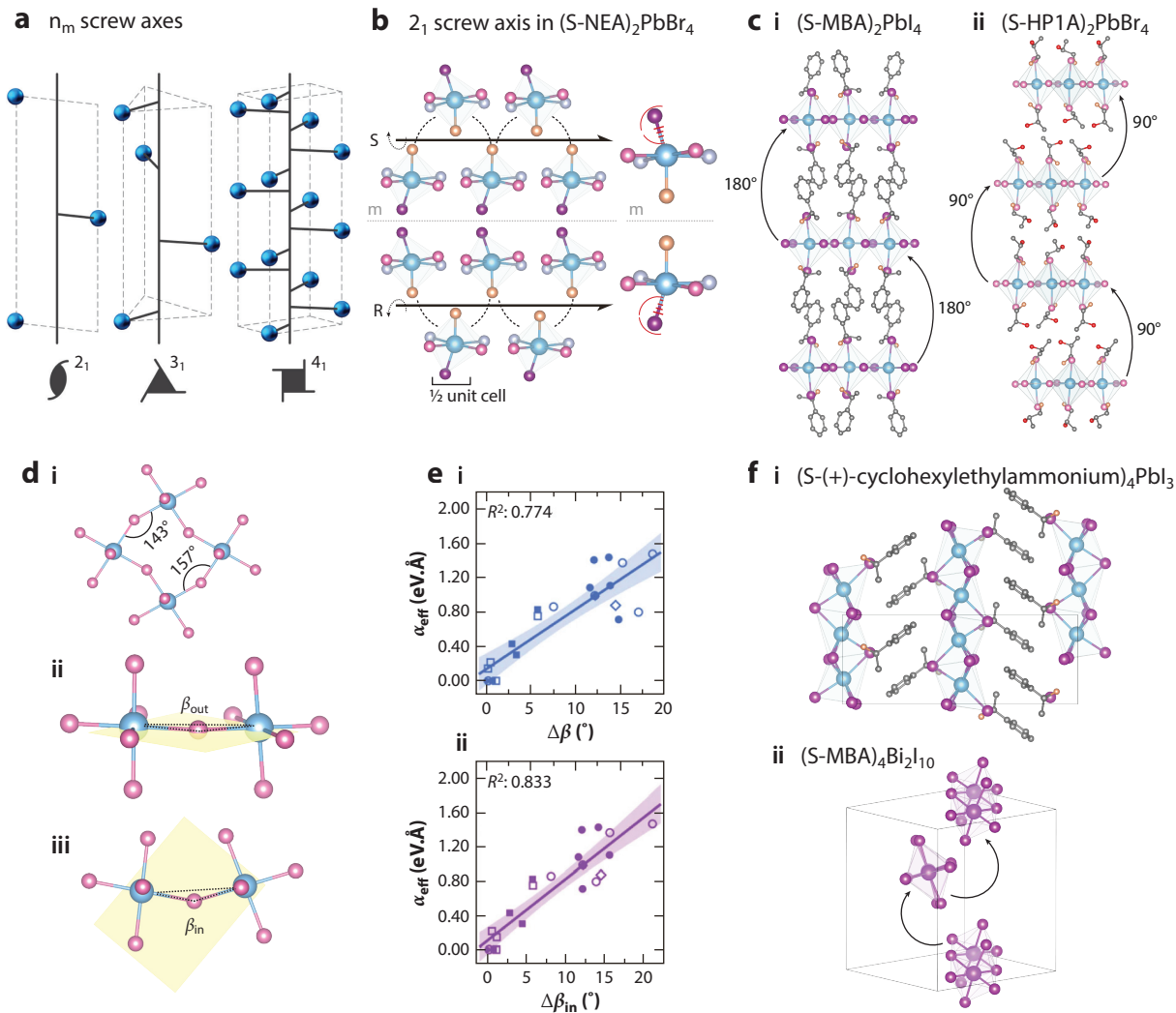


Figure 1

Selected crystal structures and parameter descriptors of 2D chiral hybrid organic-inorganic perovskite semiconductors (c-HOIS). (a) Description of the n_m screw axes and their varying translational/rotational symmetries. (b) One of the 2_1 screw axes of $(S-NEA)_2PbBr_4$ along the b axis, showing that the mirror image is nonsuperimposable. The inset on the right shows an isolated octahedron for further clarity. (c) Perovskite structures with a (i) 2_1 screw axis [$(S-MBA)_2PbI_4$; 180° rotations] in contrast to a (ii) 4_1 screw axis [$(S-HP1A)_2PbBr_4$; 90° rotations] showing the different plane twisting. (d, i) The octahedral tilting angles (β and β') in different projections used to produce (ii) β_{out} and (iii) β_{in} . (e) Correlation of (i) $\Delta\beta$ and (ii) $\Delta\beta_{in}$ with the effective Rashba-type spin splitting parameter α_{eff} . Panel e adapted from Reference 35. (f) A representative (i) 1D structure of $(S-(+)-cyclohexylethylammonium)PbI_3$ and (ii) 0D structure of $(S-MBA)_4Bi_2I_{10}$ with arrangement of the inorganic dimers along the 2_1 screw axis. β is the M-X-M bond angle, where M is the metal and X is the halide; β_{out} and β_{in} are the projections of in-plane and out-of-plane components of β ; $\Delta\beta$ is the bond angle disparity (difference), where $\Delta\beta = \beta - \beta'$; and $\Delta\beta_{in}$ is the projection of the in-plane bond angle difference.

individual octahedron is highlighted with one bromide that cannot be imposed over its mirror image. In the 2D c-HOIS structures in the $P2_1$ space group, the 2_1 screw axis is commonly parallel to the inorganic plane as is the case with the aforementioned $(S-NEA)_2PbBr_4$ (24, 28, 31). We point this out because the helical chirality associated with the screw axis may impart

anisotropic optoelectronic properties onto the inorganic framework (along the screw axis or perpendicularly). However, creative empirical results have yet to be demonstrated to probe this potential chiral anisotropy.

Unlike the 2₁ screw axis, higher n-value screw axes have enantiomorphs and make up the highest symmetry operations of the 22 chiral space groups. In higher n-value screw axes, such as 3₁ (3₂), the change in the translation distance invokes opposite enantiomers in the structure; i.e., the 1/3 versus 2/3 translation with 120° rotation produces a helix of opposite sense. A few 2D c-HOIS have been demonstrated to have a higher-fold screw axis including (R/S-HP1A)₂PbBr₄ (HP1A is 2-hydroxy-propyl-1-ammonium) and (R/S)-(BrPEA)₂PbI₄, where BrPEA is R/S-1-(4-bromophenyl)ethylammonium, which crystallize in the *P*4₁2₁2 (*P*4₃2₁2) space groups (32, 36). The 4₁ (4₃) screw axis is a 1/4 (3/4) unit cell translation followed by a 90° rotation (**Figure 1a**). In (R/S-HP1A)₂PbBr₄, the 4₁ screw axis is compensated across four inorganic layers (i.e., the unit cell is four inorganic planes tall), with each inorganic layer rotated 90° relative to one another (compared to the 180° rotation between planes in a *P*2₁2₁2₁ structure), as shown in **Figure 1c** (19). It is also worth noting that select c-HOIS structures adopt the *P*1 space group, which has no symmetry operations besides the identity (7). This extremely low symmetry has no global screw axis that can be identified, which may result in different properties than structures with a screw axis. A consideration for experimentalists going forward is if a higher n-fold screw axis modifies any measurable chirality-dependent property. It may be that properties such as the CISS effect discussed below are not dependent on the global symmetry of the crystal structure but there is more of a chirality-induced effect dependent only on the local symmetry.

It is interesting to evaluate the symmetry of the inorganic components by themselves outside of the global symmetry of the perovskite crystal structure, e.g., the symmetry of the organic and inorganic components combined. A discussion of this has been provided by Jana et al. (35) where they artificially removed the organic cations from the crystal structure of various 2D perovskites and found only some chiral structures to have transferred chirality to the inorganic planes using PLATON analysis on the inorganic component. For example, the global symmetry in (R/S-MBA)₂PbI₄ is *P*2₁2₁2₁, but upon removal of MBA, the inorganic framework adopts the *Pnma* space group (which has inversion and mirror symmetry). This is observed as a relatively flat perovskite octahedra connectivity. Furthermore, a single isolated inorganic layer of (R/S-MBA)₂PbI₄ adopts the *Pmc*2₁ space group, which has mirror symmetry and is thus achiral. Other structures, however, appear to have stronger chirality transfer in the sense that upon removal of the organic cation, the inorganic structure still lacks mirror and inversion symmetry. (S-NEA)₂PbBr₄ has a global *P*2₁ space group and maintains the *P*2₁ space group in the inorganic-only structure as well as the individual inorganic planes. Jana et al. suggested that this is related to the hydrogen bonding within the structure and that specific cations such as R/S-NEA host stronger coordination to the inorganic lattice via hydrogen bonding imparting a larger degree of structural distortion away from centrosymmetric structures. Sterics of the cation, including the degree of branching and subsequent coordination distance (i.e., distances of the ammonium head from the inorganic planes) (21), are likely components of this chirality transfer, and producing structures with the organic ammonium molecular structure being systematically varied will be interesting going forward.

We would also like to note here that symmetry evaluations of crystallographic structures are subject to interpretation. For example, the tolerances imposed on the atom distance (i.e., how far an atom can be displaced to consider a symmetry operation present, which is related to error in the measurement) during PLATON analysis can be varied, resulting in the reduction or increase of symmetry in the determined space group (37). Thus, structures may vary over analyses by different crystallographers.

PLATON:

a crystallography software package used for geometric calculations including checking for symmetry in a structure

While space groups do a good job of capturing the existence of chirality as a binary quantity (chiral or achiral), it is interesting to discuss how chiral a structure is in a quantitative way. Methods of defining the degree of chirality consist of finding distances offset of the chiral structure relative to an achiral system (38, 39). One approach, the continuous symmetry measure methodology, provides a scale between 0 and 100, where 0 is totally symmetric, providing a quantitative value for the degree of chirality. This and related methods have not been applied to halide perovskites in a comprehensive way, though some isolated structures have been evaluated for temperature-dependent chirality (40). It will be interesting to see if this can be applied in a meaningful way to c-HOIS and correlated with chiral optoelectronic properties.

In addition to the space group, there are more localized descriptions of the symmetry breaking related to the octahedral tilting. The M-X octahedron can be tilted in different directions depending on the organic cation, leading to different M-X-M bond angles β and β' , where M is the metal center and X is the halide. The difference between these angles, $\Delta\beta$, can quantify the asymmetric tilting of the octahedra within the layers (21). **Figure 1d** shows this in the chiral (S-NEA)₂PbBr₄ with two unique angles β and β' induced by the chiral cation that makes up $\Delta\beta$. In addition, there is an in-plane angle projection (β_{in}) and out-of-plane angle projection (β_{out}) providing some nuance in the directionality of the octahedral tilting (**Figure 1d**). The $\Delta\beta$ and $\Delta\beta_{\text{in}}$ parameters (**Figure 1e**) stood out among other structural descriptors as they correlate with a density functional theory calculated effective in-plane spin splitting parameter (α_{eff}) in the conduction band (CB) of the 2D perovskite (**Figure 1e**) (19). These descriptors provide some relationship between the structure and calculated spin-dependent properties, but systematic empirical results corroborating these potential structure-property relationships are yet to be demonstrated. The in-plane spin splitting is typically associated with the Rashba type of spin-orbit interactions. These are distinct from CISS in that Rashba spin splitting has a spin orientation that is perpendicular to the crystal momentum while for CISS the spin orientation and spin splitting are parallel to the momentum. This is one of the distinctions between the chiral semiconductors discussed here and chiral organic molecules. The chiral semiconductors have both long-range electronic structure and typically large spin-orbit interactions, and thus they can exhibit a variety of spin-orbit phenomena. It is not understood how, if at all, the in-plane Rashba-type spin splitting might impact out-of-plane CISS characteristics.

Another method of inducing further symmetry breaking is the recent demonstration of chiral cation mixing/doping. The chiral cation MBA-Br has been added in large amounts to achiral 2D HOIS (with linear alkylammonium) to break symmetry adopting the $P2_1$ space group (29). Furthermore, mixing chiral cations, in low concentrations referred to as chiral doping, can further break symmetries. The incorporation of (S-2-MeBA) (3.9 wt%) into (S-BrMBA)₂PbI₄ broke the symmetry from the $C2$ space group (pure structure; 0.0 wt%) to $P1$ (doped), leading to changes in the octahedral tilting. The mixing of these cations results in changes in CD spectra and may be an effective strategy for enhancing chirality-dependent properties.

It should be noted that there is also exploration of what we refer to as chiral non-perovskite hybrid metal halide structures: the 1D linear chain-like structures and 0D cluster-type structures that form when sterically restricted ammonium cations are incorporated that often contain screw axes. The structure R/S-(−/+)-(cyclohexylethylammonium)PbI₃ ($P2_1$) has a 2_1 screw axis that propagates along the linear chains of face-sharing Pb-I octahedra (8). The 0D structures are closer to crystals of molecular metal halide structures in behavior but do have some interesting packing that occurs in the structures. For example, in the (R/S-MBA)₄B₂X₁₀ (B = Sb, Bi; X = Br, I) compounds (41), there is an asymmetric distortion between the B-X dimers as well as a helical packing of the dimers (along a 2_1 screw axis) (**Figure 1f**). These structures have wider bandgaps and are

less conductive, making them less promising for electronic applications but they could be useful in chiroptical applications.

3. CHIROPTICAL PROPERTIES

3.1. Circular Dichroism

The differential absorption of left-handed circular polarization (LHCP) and right-handed circular polarization (RHCP) by a chiral medium is termed CD. For the absorption of circularly polarized light, the polarized light must couple to helical excitation or the helical motion of the electrons along the light propagation (41). CD is one of the simplest and most common methods for probing chirality. In a chiral medium, LHCP and RHCP are absorbed in different amounts; thus the propagation of linear polarized light results in an elliptical polarization (Figure 2*a,b*).

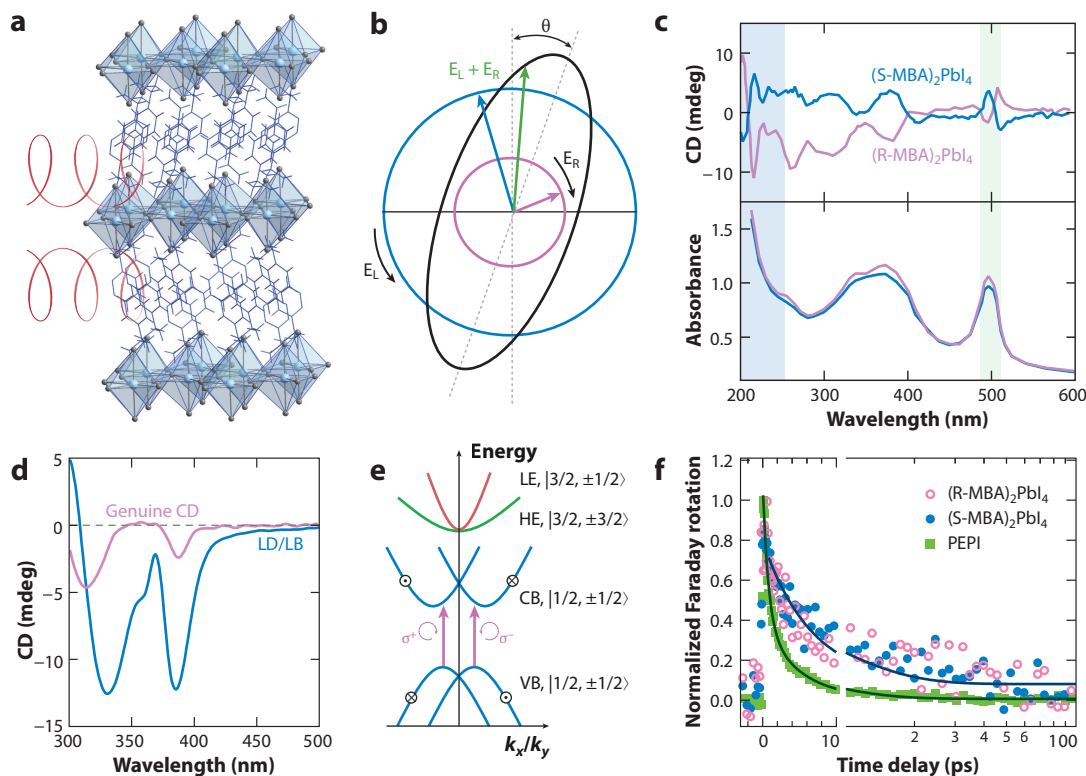


Figure 2

(*a,b*) Unequal absorption of the left (E_L)- and right (E_R)-hand polarized light leads to ellipticity. (*c*) Absorption and circular dichroism (CD) spectra of (R-MBA)₂PbI₄ and (S-MBA)₂PbI₄ hybrid organic-inorganic perovskite semiconductors (HOIS) showing opposite signs. The shaded region in green shows the Cotton effect at the band edge, and the blue shaded region indicates the CD signatures of the chiral organic cation. Panel *c* adapted with permission from Reference 2 (CC BY-NC 4.0). (*d-f*) Spin-dependent optical transitions in HOIS. (*d*) Decoupled CD spectra from the genuine CD and linear dichroism/linear birefringence (LD/LB) contribution. Panel *d* adapted with permission from Reference 46. (*e*) Schematic band diagram depicting the valence band (VB), conduction band (CB), heavy electron band (HE), and light electron band (LE) in HOIS under Rashba-type band splitting. Pink arrows represent the transitions under circularly polarized light following optical selection rules. Circles with crosses and dots inside indicate spin polarization along the z axis (along the paper). In the notation $|J, m_J\rangle$, J is the total angular momentum vector and m_J is the total angular momentum quantum number. (*f*) Time-resolved Faraday rotation characterizing spin lifetimes in (R-MBA)₂PbI₄, (S-MBA)₂PbI₄, and phenylethylammonium lead iodide (PEPI) thin films.

Generally, CD is represented by a dissymmetry factor (g_{CD}) that considers the optical absorption of the chiral film, enabling comparisons between different chiral materials:

$$g_{\text{CD}} = \text{CD (mdeg)} / (32,980 \times A),$$

where A is the absorption.

In CD spectroscopy, typically the degree ellipticity (in millidegrees) induced to a propagating beam is reported (**Figure 2b**), and the factor of 32,980 converts from millidegrees (mdeg) to ΔOD ($\text{OD}^- - \text{OD}^+$). Depending on the HOIS composition, a wide range of g_{CD} values has been reported. Typically, for the 2D c-HOIS, the g_{CD} values range from 10^{-4} to 10^{-3} (9, 42). In contrast, 1D and 0D c-HOIS have shown exceptional g_{CD} values of 10^{-2} to 10^{-1} (43, 44). These high g_{CD} values in the case of 1D and 0D HOIS need further investigation to fully understand the relationship between chiral structure and the resulting chiroptical activity. The low-energy features in the CD spectra are typically assigned to optical transitions of the metal halide framework, while the high-energy features originate from the chiral A-site cation molecules (**Figure 2c**). Derivative-like features (Cotton effect) can be observed at the band edge and may indicate lifting of the spin energy degeneracy by the addition of R/S-MBA chiral molecules (2). CD can also arise from dipole-dipole coupling (45). While CD has been a convenient technique for detecting chiroptical activity, the textured nature of c-HOIS films gives rise to phenomena that complicate the interpretation of CD. In particular, the presence of linear birefringence (LB) and linear dichroism (LD) can contribute to the CD signal and should be considered as some high observed g_{CD} values might originate from LB/LD effects (**Figure 2d**) rather than intrinsic chiral optical activity (46). c-HOIS might be suitable candidates for investigating the longstanding question of whether chiroptical activity, such as CD, can be strongly correlated with the CISS effect, owing to the tunable symmetry breaking of HOIS. Two approaches can be considered in this regard: (a) HOIS compositions with different chiral A-sites (resulting in different degrees of g_{CD}) can be compared in terms of their CISS effect to determine if any correlation exists. (b) A single HOIS composition can have its g_{CD} value tuned by chiral A-site doping or chiral amplification, and then its CISS efficiency can be compared.

3.2. Circularly Polarized Luminescence

Circularly polarized luminescence (CPL) is a complementary technique to the CD of probing chirality in the excited state by measuring the differential emission of LHCP and RHCP. Similar to g_{CD} , CPL is quantified by the luminescence dissymmetry factor g_{lum} with a theoretical limit of 2, with $g_{\text{lum}} = 2(I_{\text{L}} - I_{\text{R}})/(I_{\text{L}} + I_{\text{R}})$, where I_{L} and I_{R} represent left and right CPL, respectively. In contrast to achiral HOIS where the optical transition strengths are equal for LHCP and RHCP light, c-HOIS has unequal optical transition strength leading to CPL. 2D c-HOIS typically have low g_{lum} in the range of 10^{-5} to 10^{-3} . However, c-HOIS in the form of nanocrystals (NCs) have shown higher g_{lum} values of 10^{-2} (47). The g_{lum} not only reflects the inverse of CD but also is dependent on the excited-state dynamics. For example, if the CPL reflects the spin configuration, then g_{lum} will also encode the excited-state spin lifetime. Alternatively, high g_{lum} values approaching the theoretical limit have also been achieved by forming composites of achiral HOIS with a chiral host (48). However, such a host-guest configuration may reflect a light filtering effect rather than a chiroptical property originating from structural distortion. In the context of CISS, CPL can play an important role in understanding selective spin-polarized charge transfer. The spin-selective transport of c-HOIS has been employed in concert with 2D transition metal dichalcogenides (TMDCs) to realize valley polarization in TMDCs (49, 50). Furthermore, c-HOIS coupled with ferromagnetic (FM) layers can shed light on spin mixing and Rashba splitting. Enhancement in

CPL emissions under a magnetic field in *c*-HOIS/FM bilayers has been reported to generate chiral interfaces owing to coupling between the HOIS and ferromagnet, manifesting CISS (51). We anticipate CISS-based single-photon CPL in *c*-HOIS in the near future offering the transduction of chiral information into photonic devices (52).

3.3. Spin Lifetimes

The large spin-orbit coupling that can result in phenomena such as Rashba spin splitting, CISS, and large optically oriented spin polarization in HOIS makes them promising for spin optoelectronic applications. To fully realize the potential of spin-dependent characteristics in HOIS, it is important to measure and control their spin lifetimes. The unique electronic band structure in HOIS allows the optical excitation and detection of spin-polarized carriers. **Figure 2e** shows the schematic band diagram for HOIS under in-plane Rashba-type band splitting where the valence band (VB) and CB have $|J, m_J\rangle$ states of $|1/2, \pm 1/2\rangle$. While the VB is filled with equal amounts of spin-up and spin-down states in the ground state, LHCP or RHCP (σ^+/σ^-) carrying an angular momentum of ± 1 allows the selective optical excitation of spin-polarized carriers in accordance with angular momentum conservation ($\Delta m_J = \pm 1$). To date, a few time-resolved pump-probe spectroscopy tools have been applied to measure spin lifetimes in HOIS, including circularly polarized transient absorption (CPTA) or reflection (53–57) and time-resolved Faraday (or Kerr) rotation (TRFR) (58). Varying the time delay between the pump and probe can map out the relaxation dynamics of spin-polarized carriers as functions of energy and time. Spin relaxation is typically described by the spin relaxation time T_1 and spin dephasing time T_2^* , where CPTA and TRFR can elucidate the spin relaxation time T_1 , while T_2^* can be measured by applying a longitudinal magnetic field since optical orientation produces a spin orientation along the beam propagation direction (59).

3D HOIS have been reported to have spin lifetimes of a few picoseconds at room temperature and beyond nanoseconds at cryogenic temperatures (54, 58). The spin lifetime of 2D HOIS was found to increase with decreasing exciton binding energy and increasing layer thickness (55, 56). We have measured spin lifetimes in (R-MBA)₂PbI₄, (S-MBA)₂PbI₄, and phenylethylammonium lead iodide (PEPI) thin films using TRFR. As shown in **Figure 2f**, optically oriented spin-polarized carriers in PEPI decay with a lifetime of 5.2 ps, whereas (R-MBA)₂PbI₄ and (S-MBA)₂PbI₄ exhibit a much longer spin lifetime of ~ 20 ps. Recently, Liu et al. (30) reported a microsecond spin polarization lifetime in a 2D *c*-HOIS 3BrMBA₂PbI₄ and also exhibited a high degree of CPL of up to 52%.

In addition to time-resolved pump-probe measurements, steady-state measurements such as the optical Hanle effect have also been used to extract spin lifetimes (60). Typically, the optical Hanle effect employs measuring the degree of CPL under continuous excitation while applying a magnetic field transverse to the spin orientation. The degree of CPL reflects the spin polarization of carriers. Magneto-optical measurements, including magneto CPL, magneto circularly polarized electroluminescence, and magneto photoconductivity, are another class of optical tools to assess the spin relaxation and lifetime. For example, using magneto CPL measurements and a microscopic model incorporating natural optical activity and spin transport for *c*-HOIS, the spin lifetime for (R/S-MBA)₂PbI₄ was found to be 20 ps at 4 K (61, 62). Moving forward, the random orientation of crystallites in polycrystalline *c*-HOIS thin films needs to be considered when comparing spin lifetimes. Whether the spin lifetime has any impact on the charge-to-spin current conversion efficiency under CISS remains an open question. There are two important distinctions to consider when comparing the measured spin lifetimes to CISS: (a) In the CISS configuration,

only one type of carrier is present, electrons or holes, while for optical measurements both types are typically present. The strong exchange interaction inherent in quantum confined systems can dominate spin relaxation even at room temperature (55). Thus, optical measurements may not represent the isolated electron or hole spin relaxation phenomena. (b) In CISS, the spin that matches the chirality is the majority spin, and when under an applied bias any spin scattering must also result in a change in momentum.

4. MEASURING CHIRALITY-INDUCED SPIN SELECTIVITY

4.1. Magnetic Conductive Probe Atomic Force Microscopy

The original observation of CISS involved using photoelectron emission spectroscopy where polarized electrons ejected from Au substrates scatter differently depending on the chirality of an organic monolayer (1). Since then, many experimental methods have been developed for observing and investigating the CISS effect. Particularly common is magnetic conductive probe atomic force microscopy (mcp-AFM) where current is passed through a chiral layer with one of the contacts [either an atomic force microscopy (AFM) tip or conductive substrate] being FM (63). Based on the magnetization of the FM contact, spin-up or spin-down carriers are detected (**Figure 3a**). The CISS effect produces the polarization of spin-up (-down) carriers, and the preferential transmission into the FM layer results in distinct current-voltage (I-V) curves (**Figure 3b,c**) depending on the magnetization and chirality type. The spin polarization is defined as $P_s = (I^\uparrow - I^\downarrow)/(I^\uparrow + I^\downarrow)$, where $I^{\uparrow/\downarrow}$ refers to the current measured when the ferromagnet is polarized up or down. Various structures of c-HOIS have been measured with this technique; however, trends in the spin selectivity have yet to emerge (2, 25, 32, 64–66). In c-HOIS, $|P_s|$ has been reported to be as high as 94% and as low as 50%, which are undoubtedly large for a nonmagnetic material, but there is no clear mechanism for the measured differences and no clear design rules about what structural factors are important (25, 32).

Here, we aim to clarify the technique for mcp-AFM of c-HOIS and suggest some best practices. First, the two-terminal measurement involves a metallic FM in contact with the semiconducting c-HOIS. During the measurement, there is band bending at the interface to match the metal's work function and semiconductor Fermi level (i.e., a Schottky junction). It is not clear what effect, if any, this Schottky junction has on the detection of spin-polarized carriers. Often, multiple points are selected for data collection, and a large number of I-V curves are independently averaged for I^\uparrow and then for I^\downarrow as individual I-V curves can be fairly noisy; P_s is determined from these averaged curves. Thus, I^\uparrow and I^\downarrow measurements do not typically probe the same location on the film, and variations in crystal grain structures, film thicknesses, defects, etc. are averaged out. We recommend that maps or line scans should be done systematically on samples to produce more reliable I-V curve statistics, which avoids bias in point sampling. Furthermore, the choice of FM contact may have some impact, particularly using the AFM tip as the ferromagnet draws into question the time that the polarization is held as well as the spin orientation. Experiments employing ferromagnet substrates under an applied magnetic field are seemingly more reliable as there is no loss in polarization during the measurement. Furthermore, cross-checking the mcp-AFM experiments with magnetoresistance (MR) (discussed below) can be extremely valuable, as there are differences in the magnitude of the observed CISS effect.

4.2. Half-Spin Valves

A spin valve is a microelectronic device in which high- and low-resistance states are realized by using both the charge and spin of carriers. In traditional spin valves, two FM electrodes with

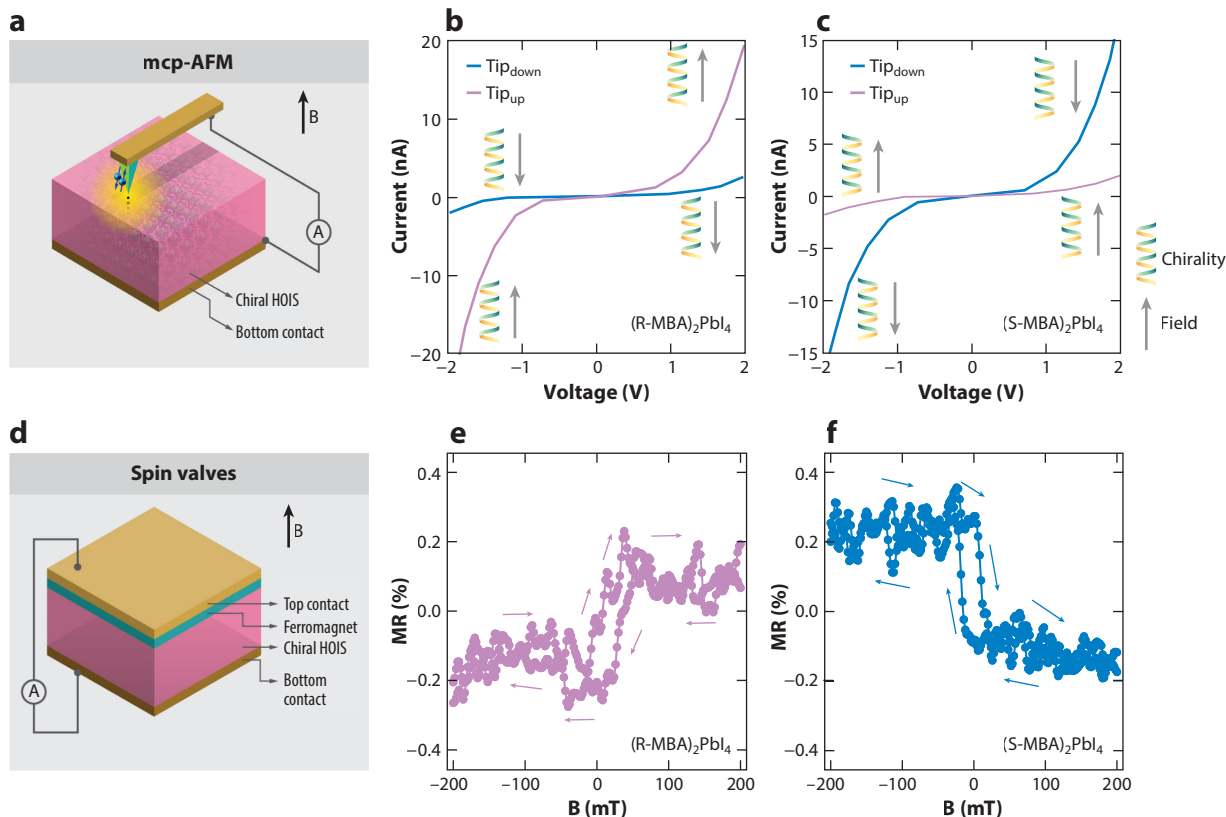


Figure 3

(a) Schematic architecture of mcp-AFM. Room-temperature current voltage curves obtained using the mcp-AFM technique of 2D c-HOIS thin films for (b) $(R\text{-MBA})_2\text{PbI}_4$ and (c) $(S\text{-MBA})_2\text{PbI}_4$. (d) Schematic architecture of spin valves. MR response of spin valves based on (e) $(R\text{-MBA})_2\text{PbI}_4$ and (f) $(S\text{-MBA})_2\text{PbI}_4$. The device architecture consisted of ITO/HOIS/NiFe. Abbreviations: A, current; B, magnetic field; HOIS, hybrid organic-inorganic perovskite semiconductors; mcp-AFM, magnetic conductive probe atomic force microscopy; MR, magnetoresistance. Panels b, c, e, and f adapted with permission from Reference 2 (CC BY-NC 4.0).

different coercivities sandwich a nonmagnetic conductor. As the external magnetic field is varied, the magnetic polarization of the two FM electrodes will be either parallel (coaligned) or antiparallel; when the two FM are coaligned the device exhibits a low resistance state, and when antiparallel it is in a high resistance state (67). Incorporating a chiral layer that exhibits CISS removes the need for one of the FM and thus is a half-spin valve, with the other electrode being a nonmagnetic contact to the CISS material. The resistance state depends on whether the FM is aligned up or down and on the chirality of the chiral layer (**Figure 3d**). In principle, the half-spin valve is functionally the same as the mcp-AFM experiment with the FM being either the AFM tip or the substrate. However, in the spin-valve experiment, the resistance is measured as a function of the applied magnetic field. In such c-HOIS half-spin valves, the MR response follows the hysteresis loop of the FM electrode (2). Spin-polarized carriers from an FM electrode experience CISS while passing through the c-HOIS layer, leading to an opposite MR response for left- and right-handed HOIS (**Figure 3e,f**). The highest CISS-based MR response reported for c-HOIS is around 0.9% with the HOIS crystal structure exhibiting fourfold symmetry (68). Such a low MR for c-HOIS is perplexing as the spin polarization measured by mcp-AFM can be as high as 94%

(25). Such a discrepancy can be due to several reasons such as a low-quality interface leading to inefficient spin injection, conductivity mismatch between the FM and semiconducting HOIS (69), an overestimation of spin polarization in mcp-AFM measurements, and the electronic instability of HOIS arising from ion migration. The FM electrode–HOIS interface plays a critical role in determining the spin valve efficacy, and it is possible that traditionally used metallic FM layers may not be the best candidates for HOIS spin valves. Typically, there is a conductivity mismatch between the FM electrode and HOIS that is rectified by adding a tunneling barrier between the two layers. This tunneling barrier is crucial in determining the spin injection efficiency from the FM electrode to HOIS. The tunneling barrier thickness and material selection need to be considered while designing HOIS spin valves, which has not received any attention so far. Other FM electrodes such as dilute magnetic semiconductors (DMS) can be explored for improved spin interfaces (70). CISS-based HOIS spin valves are still in their infancy, and we envision future advances in the direction of more stable c-HOIS compositions, better spin valve interfaces and architectures, and advanced MR measurement techniques considering HOIS electronic stability.

4.3. Spin Light-Emitting Diodes

Spin light-emitting diodes (LEDs) are circularly polarized LEDs based on the injection of spin-polarized currents into a semiconducting emitter layer. The original spin LEDs were based on an FM/tunnel oxide/semiconductor or dilute magnetic semiconductors (DMS)/semiconductor heterointerface (71–73). The FM or DMS, when magnetically polarized, injects spin-polarized carriers into the semiconductor where light is emitted via electron-hole pair recombination. Due to the optical selection rules, $\Delta m_J = \pm 1$, the electron and hole must have the same spin to recombine, and when there is spin accumulation of either the electron or hole, the emission will also be circularly polarized since the angular momentum is transferred to the photon. In fact, the degree of circular polarization of the electroluminescence is directly related to the degree of spin accumulation in the emitter layer. The degree of circular polarization P_{cp} is defined as $P_{cp} = (I_L - I_R)/(I_L + I_R)$, where I_L (I_R) is the intensity of left (right)-handed circular polarized light emitted. P_{cp} can be related to three parameters, $P_{cp} = \alpha \cdot F \cdot P_{inj}$, where α is determined by the optical selection rules ranging from 0.5 to 1, F is the fraction of spin-polarized carriers that emit prior to spin relaxation, $F = \frac{1}{(1+\tau/\tau_s)}$, where τ is the total carrier lifetime and τ_s is the spin lifetime, and P_{inj} is the spin injection efficiency into the emitter (74, 75).

The CISS effect has been utilized to produce a spin LED without the need for FM or DMS that operates at room temperature with no applied magnetic field. In the first CISS-based demonstration, $(R/S\text{-MBA})_2\text{PbI}_4$ was used as a spin injector coupled with $\text{CsPb}(\text{Br}_{1-x}\text{I}_x)_3$ emitter NCs (3). The completed LED emitted circularly polarized light by spin injection from $(R/S\text{-MBA})_2\text{PbI}_4$ into the $\text{CsPb}(\text{Br}_{1-x}\text{I}_x)_3$ NCs, which were in direct contact with one another, and no buffer layer was intentionally added to the structure. The LED shows P_{cp} of 2.6% and is mainly limited by the short spin lifetime ($\tau_s \sim 14$ ps) of the nonchiral emitting NCs. This work, combining c-HOIS with other halide perovskite emitters as spin LEDs, has been expanded upon by multiple researchers (76–80). There have been some interesting demonstrations for polarized light emission, such as core/shell NCs where the core is an achiral emitter and the shell is a chiral component (77) or the example of a spin funneling mechanism where the spin polarization is transferred from chiral components to achiral components prior to light emission (76).

Recently, a spin LED (**Figure 4a**) based on the integration of c-HOIS with a conventional III-V AlGaInP multiquantum well (MQW) LED was demonstrated that exhibited large P_{cp} (**Figure 4b**) (75). A key experimental demonstration was the optical Hanle effect where an applied magnetic field produces spin depolarization and subsequent reduction of the observable

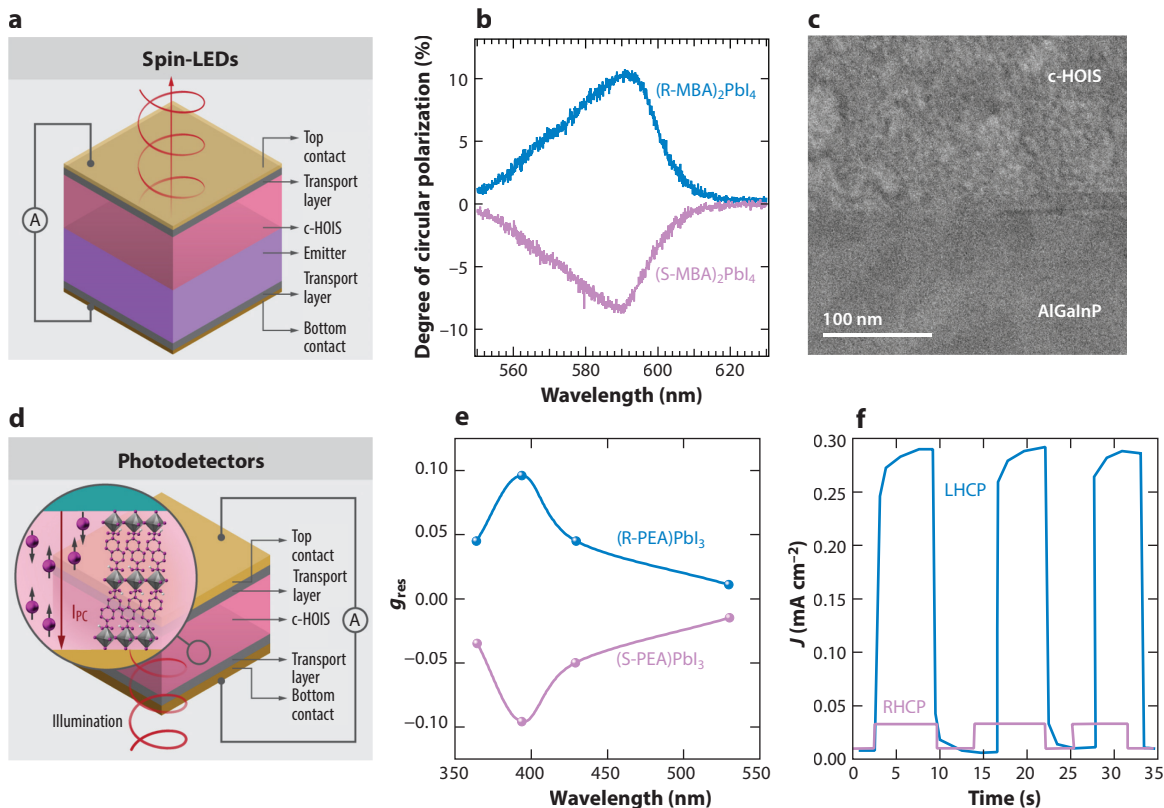


Figure 4

(a) Schematic architecture of spin-LEDs. (b) Left and right circularly polarized luminescence emission from spin-LEDs with (R/S-MBA)₂PbI₄ as the spin filter. (c) Cross-sectional transmission electron microscopy images of the AlGaInP/c-HOIS interface. Panels b and c adapted with permission from Reference 75. (d) Schematic architecture of CPPs. (e) Anisotropic responsivity (g_{res}) for (R-PEA)PbI₃ and (S-PEA)PbI₃. Panel e adapted from Reference 81 (CC BY 4.0). (f) Time-dependent CPP response for LHCP and RHCP using (R-NEA)PbI₃ HOIS. Panel f adapted from Reference 43 (CC BY-NC 4.0). Abbreviations: A, current; c-HOIS, chiral HOIS; CPP, circularly polarized photodetector; HOIS, hybrid organic-inorganic perovskite semiconductors; LED, light-emitting diode; LHCP, left-handed circular polarization; RHCP, right-handed circular polarization.

P_{cp} , clearly indicating that the circularly polarized emission is the result of spin injection and spin accumulation in the achiral III-V emitter layer. In the c-HOIS/III-V spin LED, spin-polarized holes are injected from the c-HOIS into the MQW III-V emitter layer through a 200-nm cladding layer. P_{inj} was determined to be between $\sim 25\%$ and 50% , which contains both the contribution from CISS and any spin scattering in the cladding layer during transport. This suggests there is no fundamental limitation to spin injection across the interface of c-HOIS and III-V or other conventional semiconductors (Figure 4c shows a transmission electron microscopy image of this interface). This result demonstrates that incorporating the c-HOIS layer into standard semiconductor structures can enable spin control in traditional optoelectronics.

More broadly, spin LEDs provide an excellent method of observing spin polarization resulting from CISS that does not rely on metallic FM/semiconductor contacts. As more platforms of CISS-based spin LEDs are developed, this may be a key method for the evaluation of the CISS effect. The semiconductor/semiconductor interface and nonmagnetic detection allow for better

probing of the CISS effect, avoiding the aforementioned conductivity mismatch (69) between FM and semiconductors lending a simpler interface to the model. In addition, spin LEDs have the potential for high-throughput device fabrication, with the goal of testing various parameters that impact the CISS effect such as alternating current, voltage, structural chemistry, the thickness of the spin injector, and semiconductor band offset. Specifically, solution-processed spin LEDs are possible (akin to quantum dot LEDs), where a significant number of devices can be made, allowing researchers to probe the operating properties in better detail.

4.4. Circularly Polarized Photodetectors

In circularly polarized photodetectors (CPPs), spin-polarized carriers are generated upon excitation with circularly polarized light due to optical selection rules (**Figure 4d**). CPPs have attracted significant interest in recent years owing to their emerging applications in machine vision, remote sensing, and quantum optics. Significant progress has been made in c-HOIS-based CPPs covering ultraviolet to near-infrared regimes (81–83). It is interesting to note that CPPs based on 1D c-HOIS exhibit high performance consistent with their high CD (**Figure 4e,f**). Spin-polarized carriers generated under circularly polarized light experience different transport drift depending on the chirality of the HOIS layer based on the CISS effect. The architecture of CPPs does not consist of any FM electrode nor do they need a magnetic field to operate, making them a simple and convenient platform for investigating the CISS effect. However, a major drawback of CPPs is the lack of metrics to quantify CISS. Nonetheless, the performance of CPPs can be quantified using the established performance metrics such as responsivity. For conventional photodetectors, responsivity (R) is a key metric and is expressed as $R = \Delta I / (P \cdot S)$, where ΔI is the difference between the photocurrent and the dark current, P is the incident power density, and S is the effective illuminated area. For CPPs, considering the unequal absorption of LHCP and RHCP, an anisotropic responsivity can be defined as $g_{\text{res}} = (R_L - R_R) / (R_L + R_R)$, where R_L and R_R are the responsivities under LHCP and RHCP, respectively. Conventional metrics used for HOIS photodetectors such as the on/off ratio, responsivity, photo gain, external quantum efficiency, and detectivity have yet to be systematically applied to c-HOIS CPPs.

4.5. Spin Seebeck Effect

Magnetic materials exhibit the spin Seebeck effect where a thermal gradient generates a spin current from the hot to the cold side (84). Recently, Kim et al. (5) suggested that the propagation of chiral phonons in the absence of magnetization can lead to spin injection from the c-HOIS to a proximal nonmagnetic metal layer, known as the chiral-phonon-activated spin Seebeck (CPASS) effect. Chiral phonons are a collective vibrational pattern arising from the circular orbital motions of atoms around their equilibrium lattice positions (85–87). In CPASS measurements, a temperature gradient is applied to a heterostructure involving a c-HOIS layer and a metal layer to drive the propagation of chiral phonons, as shown in **Figure 5a**. A nonequilibrium spin current is generated in the metal layer with the spin orientation aligning parallel to the direction of the thermal gradient. Kim et al. suggested that the coupling between magnons and phonons allows the transfer of spin angular momentum to the metal layer given the conservation of angular momentum. Time-resolved Kerr rotation measurements show that the spin polarization in the metal layer is dependent on the chirality of the HOIS layer, where the phase of the time-resolved magneto-optical Kerr effect changes sign as the chirality changes from R to S (**Figure 5b,c**). The spin Seebeck is not only useful for the spin caloritronic but is also valuable for addressing the role and presence of chiral phonons in c-HOIS.

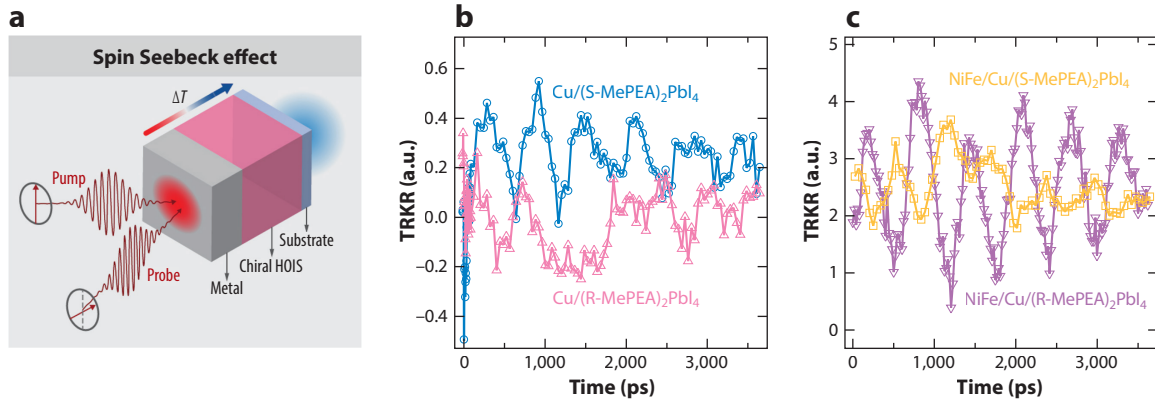


Figure 5

(a) Schematic for chiral-phonon-activated spin Seebeck effect measured via TRKR measurements. (b) Room-temperature TRKR signals on the Cu layer side for $\text{Cu}/(\text{S-MePEA})_2\text{PbI}_4$ and $\text{Cu}/(\text{R-MePEA})_2\text{PbI}_4$ thin films, respectively. (c) Room-temperature TRKR signals for $\text{NiFe}/\text{Cu}/(\text{S-MePEA})_2\text{PbI}_4$ and $\text{NiFe}/\text{Cu}/(\text{R-MePEA})_2\text{PbI}_4$ thin films, respectively. Panels b and c adapted with permission from Reference 5. Abbreviations: HOIS, hybrid organic-inorganic perovskite semiconductors; TRKR, time-resolved Kerr rotation.

5. OUTLOOK

Chirality as a general topic has been explored and investigated for over 100 years in both the chemistry and physics communities. Chemists understand chirality in terms of molecular and supramolecular structure, while physicists understand how the lack of parity (lack of inversion symmetry in three dimensions) impacts fundamental physical behavior. CISS joins these two communities through the realization that structural chirality can impact the electron spin. A stationary electron is not chiral; however, a moving electron traces out a helical path whose chirality depends on the spin orientation. While currently there is no general theoretical consensus that can accurately describe all the CISS-based phenomena, c-HOIS offer a unique platform for the testing of various hypotheses. c-HOIS also provide a unique hybrid chiral semiconducting platform for realizing the benefits of CISS in optoelectronic applications. However, there is no consensus on the specific design rules or guidelines for CISS in c-HOIS. For example, how thick should the c-HOIS layer be? Does the CISS spin polarization efficiency scale with g_{CD} or g_{lum} ? How does the spin lifetime within the c-HOIS layer impact spin transport or spin polarization efficiency? What impact, if any, does in-plane Rashba-type spin splitting play? Is the orientation of the chiral organic cations or the global crystal chirality more important? Is a 2_1 or 4_2 screw axis better for CISS?

In this review we attempted to provide a primer on the different potential knobs that c-HOIS offer for varying structural chirality. We provided an overview of the various CISS demonstrations, devices, and measurements in c-HOIS. It is our perspective that as more researchers develop new ways of interrogating CISS, creating innovative chiral hybrid systems, and incorporating them into various device structures, our understanding of CISS will also increase. Chiral hybrid organic-inorganic semiconductors represent a novel class of chiral systems for CISS and spin polarization. The juxtaposition of the organic and inorganic components provides unique flexibility and functionality for testing hypotheses and driving novel concepts.

DISCLOSURE STATEMENT

The authors are not aware of any affiliations, memberships, funding, or financial holdings that might be perceived as affecting the objectivity of this review.

ACKNOWLEDGMENTS

We are grateful for the many discussions about chirality in metal halide semiconductors with colleagues at the Center for Hybrid Organic Inorganic Semiconductors for Energy (CHOISE), including Dali Sun, Valy Vardeny, Pete Sercel, Joseph Luther, Jeffery Blackburn, David Mitzi, Young-Hoon Kim, and Haipeng Lu. This work was supported as part of the CHOISE Energy Frontier Research Center funded by the Office of Basic Energy Sciences, Office of Science within the US Department of Energy (DOE). This work was authored in part by the National Renewable Energy Laboratory, operated by Alliance for Sustainable Energy, LLC, for DOE under contract DE-AC36-08GO28308. The views expressed in the article do not necessarily represent the views of the DOE or the US government.

LITERATURE CITED

1. The first paper demonstrating chirality-induced spin selectivity effect.

2. The first demonstration of spin-dependent charge transport in chiral halide perovskite semiconductors.

3. The first demonstration of incorporating a chiral halide perovskite to make a spin LED.

5. The first demonstration of how chiral phonons generate spin currents in chiral halide perovskite semiconductors.

9. The first demonstration of chiral optical activities in chiral halide perovskite semiconductors.

1. Ray K, Ananthavel SP, Waldeck DH, Naaman R. 1999. Asymmetric scattering of polarized electrons by organized organic films of chiral molecules. *Science* 283:814–16
2. Lu H, Wang J, Xiao C, Pan X, Chen X, et al. 2019. Spin-dependent charge transport through 2D chiral hybrid lead-iodide perovskites. *Sci. Adv.* 5:eaay0571
3. Kim Y-H, Zhai Y, Lu H, Pan X, Xiao C, et al. 2021. Chiral-induced spin selectivity enables a room-temperature spin light-emitting diode. *Science* 371:1129–33
4. Kim JY, Lee J-W, Jung HS, Shin H, Park N-G. 2020. High-efficiency perovskite solar cells. *Chem. Rev.* 120:7867–918
5. Kim K, Vetter E, Yan L, Yang C, Wang Z, et al. 2023. Chiral-phonon-activated spin Seebeck effect. *Nat. Mater.* 22:322–28
6. Wang T, Sun H, Li X, Zhang L. 2024. Chiral phonons: prediction, verification, and application. *Nano Lett.* 24:4311–8
7. Huang P-J, Taniguchi K, Miyasaka H. 2019. Bulk photovoltaic effect in a pair of chiral-polar layered perovskite-type lead iodides altered by chirality of organic cations. *J. Am. Chem. Soc.* 141:14520–3
8. Hu Y, Florio F, Chen Z, Phelan WA, Siegler MA, et al. 2020. A chiral switchable photovoltaic ferroelectric 1D perovskite. *Sci. Adv.* 6:eaay4213
9. Ahn J, Lee E, Tan J, Yang W, Kim B, Moon J. 2017. A new class of chiral semiconductors: chiral-organic-molecule-incorporating organic-inorganic hybrid perovskites. *Mater. Horiz.* 4:851–56
10. Ma J, Fang C, Chen C, Jin L, Wang J, et al. 2019. Chiral 2D perovskites with a high degree of circularly polarized photoluminescence. *ACS Nano* 13:3659–65
11. Žutić I, Fabian J, Das Sarma S. 2004. Spintronics: fundamentals and applications. *Rev. Mod. Phys.* 76:323–410
12. Jansen R. 2012. Silicon spintronics. *Nat. Mater.* 11:400–8
13. Fecher GH, Kübler J, Felser C. 2022. Chirality in the solid state: chiral crystal structures in chiral and achiral space groups. *Materials* 15:5812
14. Manser JS, Christians JA, Kamat PV. 2016. Intriguing optoelectronic properties of metal halide perovskites. *Chem. Rev.* 116:12956–3008
15. Yin W-J, Shi T, Yan Y. 2014. Unusual defect physics in CH₃NH₃PbI₃ perovskite solar cell absorber. *Appl. Phys. Lett.* 104:063903
16. Mao L, Stoumpos CC, Kanatzidis MG. 2019. Two-dimensional hybrid halide perovskites: principles and promises. *J. Am. Chem. Soc.* 141:1171–90
17. Saparov B, Mitzi DB. 2016. Organic-inorganic perovskites: structural versatility for functional materials design. *Chem. Rev.* 116:4558–96
18. Long G, Sabatini R, Saidaminov MI, Lakhwani G, Rasmita A, et al. 2020. Chiral-perovskite optoelectronics. *Nat. Rev. Mater.* 5:423–39
19. Billing DG, Lemmerer A. 2006. Synthesis and crystal structures of inorganic-organic hybrids incorporating an aromatic amine with a chiral functional group. *CrystEngComm* 8:686–95
20. Billings D. 2013. Inorganic-organic hybrids incorporating a chiral cyclic ammonium cation. *S. Afr. J. Chem.* 66:263–72

21. Du K, Tu Q, Zhang X, Han Q, Liu J, et al. 2017. Two-dimensional lead(II) halide-based hybrid perovskites templated by acene alkylamines: crystal structures, optical properties, and piezoelectricity. *Inorg. Chem.* 56:9291–302
22. Rekiş T. 2020. Crystallization of chiral molecular compounds: what can be learned from the Cambridge Structural Database? *Acta Crystallogr. B* 76:307–15
23. Ding Z, Chen Q, Jiang Y, Yuan M. 2024. Structure-guided approaches for enhanced spin-splitting in chiral perovskite. *JACS Au* 4:1263–77
24. Li D, Liu X, Wu W, Peng Y, Zhao S, et al. 2021. Chiral lead-free hybrid perovskites for self-powered circularly polarized light detection. *Angew. Chemie Int. Ed.* 60:8415–18
25. Lu H, Xiao C, Song R, Li T, Maughan AE, et al. 2020. Highly distorted chiral two-dimensional tin iodide perovskites for spin polarized charge transport. *J. Am. Chem. Soc.* 142:13030–40
26. Zhu T, Weng W, Ji C, Zhang X, Ye H, et al. 2022. Chain-to-layer dimensionality engineering of chiral hybrid perovskites to realize passive highly circular-polarization-sensitive photodetection. *J. Am. Chem. Soc.* 144:18062–68
27. Xie Y, Morgenstein J, Bobay BG, Song R, Caturello NAMS, et al. 2023. Chiral cation doping for modulating structural symmetry of 2D perovskites. *J. Am. Chem. Soc.* 145:17831–44
28. Fan C-C, Han X-B, Liang B-D, Shi C, Miao L-P, et al. 2022. Chiral Rashba ferroelectrics for circularly polarized light detection. *Adv. Mater.* 34:2204119
29. Yan L, Jana MK, Sercel PC, Mitzi DB, You W. 2021. Alkyl-aryl cation mixing in chiral 2D perovskites. *J. Am. Chem. Soc.* 143:18114–20
30. Liu S, Kepenekian M, Bodnar S, Feldmann S, Heindl MW, et al. 2023. Bright circularly polarized photoluminescence in chiral layered hybrid lead-halide perovskites. *Sci. Adv.* 9:eadh5083
31. Jana MK, Song R, Liu H, Khanal DR, Janke SM, et al. 2020. Organic-to-inorganic structural chirality transfer in a 2D hybrid perovskite and impact on Rashba-Dresselhaus spin-orbit coupling. *Nat. Commun.* 11:4699
32. Abhervé A, Mercier N, Kumar A, Das TK, Even J, et al. 2023. Chirality versus symmetry: electron's spin selectivity in nonpolar chiral lead-bromide perovskites. *Adv. Mater.* 35:2305784
33. Dryzun C, Avnir D. 2012. On the abundance of chiral crystals. *Chem. Commun.* 48:5874–76
34. Flack HD. 2003. Chiral and achiral crystal structures. *Helv. Chim. Acta* 86:905–21
35. **Jana MK, Song R, Xie Y, Zhao R, Sercel PC, et al. 2021. Structural descriptor for enhanced spin-splitting in 2D hybrid perovskites. *Nat. Commun.* 12:4982**
36. Huang P-J, Taniguchi K, Shigefuji M, Kobayashi T, Matsubara M, et al. 2021. Chirality-dependent circular photogalvanic effect in enantiomorphic 2D organic-inorganic hybrid perovskites. *Adv. Mater.* 33:2008611
37. Mihalyi-Koch W, Guo S, Dai Z, Pan D, Lafayette DP II, et al. 2024. Revealing hidden non-centrosymmetry in globally centrosymmetric 2D halide perovskites. *Chem* 10:2180–95
38. Dryzun C, Zait A, Avnir D. 2011. Quantitative symmetry and chirality—a fast computational algorithm for large structures: proteins, macromolecules, nanotubes, and unit cells. *J. Comput. Chem.* 32:2526–38
39. Buda AB, Mislow K. 1992. A Hausdorff chirality measure. *J. Am. Chem. Soc.* 114:6006–12
40. Pols M, Brocks G, Calero S, Tao S. 2024. Temperature-dependent chirality in halide perovskites. *J. Phys. Chem. Lett.* 15:8057–64
41. Maughan AE, Koknat G, Sercel PC, Jana MK, Brunecky R, et al. 2023. Impact of chiral symmetry breaking on spin-texture and lone pair expression in chiral crystals of hybrid antimony and bismuth halides. *Chem. Mater.* 35:9086–101
42. Son J, Ma S, Jung YK, Tan J, Jang G, et al. 2023. Unraveling chirality transfer mechanism by structural isomer-derived hydrogen bonding interaction in 2D chiral perovskite. *Nat. Commun.* 14:3124
43. Ishii A, Miyasaka T. 2020. Direct detection of circular polarized light in helical 1D perovskite-based photodiode. *Sci. Adv.* 6:eabd3274
44. Hao J, Lu H, Mao L, Chen X, Beard MC, Blackburn JL. 2021. Direct detection of circularly polarized light using chiral copper chloride-carbon nanotube heterostructures. *ACS Nano* 15:7608–17
45. Nordén B, Rodger A, Dafforn T. 2010. *Linear Dichroism and Circular Dichroism: A Textbook on Polarized-Light Spectroscopy*. Cambridge, UK: Royal Soc. Chem.

35. Evaluation of symmetry and different structure-spin property relationships.

46. How to correctly extract circular dichroism in chiral halide perovskite semiconductors.

46. Zhang Z, Wang Z, Sung HH, Williams ID, Yu ZG, Lu H. 2022. Revealing the intrinsic chiroptical activity in chiral metal-halide semiconductors. *J. Am. Chem. Soc.* 144:22242–50
47. Kim Y-H, Zhai Y, Gauldin EA, Habisreutinger SN, Moot T, et al. 2020. Strategies to achieve high circularly polarized luminescence from colloidal organic–inorganic hybrid perovskite nanocrystals. *ACS Nano* 14:8816–25
48. Liu S, Liu X, Wu Y, Zhang D, Wu Y, et al. 2022. Circularly polarized perovskite luminescence with dissymmetry factor up to 1.9 by soft helix bilayer device. *Matter* 5:2319–33
49. Chen Y, Ma J, Liu Z, Li J, Duan X, Li D. 2020. Manipulation of valley pseudospin by selective spin injection in chiral two-dimensional perovskite/monolayer transition metal dichalcogenide heterostructures. *ACS Nano* 14:15154–60
50. Shrestha S, Li M, Park S, Tong X, DiMarzio D, Cotlet M. 2023. Room temperature valley polarization via spin selective charge transfer. *Nat. Commun.* 14:5234
51. Pan R, Tang X, Wang X, Liu Y, Huang L, et al. 2024. Impact of chiral spinterfaces on magneto-photoluminescence effects for chiral lead halide perovskites. *ACS Appl. Mater. Interfaces* 16:2964–71
52. Mishra S, Bowes EG, Majumder S, Hollingsworth JA, Htoon H, Jones AC. 2024. Inducing circularly polarized single-photon emission via chiral-induced spin selectivity. *ACS Nano* 18:8663–72
53. Giovanni D, Lim JWM, Yuan Z, Lim SS, Righetto M, et al. 2019. Ultrafast long-range spin-funneling in solution-processed Ruddlesden–Popper halide perovskites. *Nat. Commun.* 10:3456
54. Giovanni D, Ma H, Chua J, Grätzel M, Ramesh R, et al. 2015. Highly spin-polarized carrier dynamics and ultralarge photoinduced magnetization in $\text{CH}_3\text{NH}_3\text{PbI}_3$ perovskite thin films. *Nano Lett.* 15:1553–58
55. Chen X, Lu H, Wang K, Zhai Y, Lunin V, et al. 2021. Tuning spin-polarized lifetime in two-dimensional metal–halide perovskite through exciton binding energy. *J. Am. Chem. Soc.* 143:19438–45
56. Chen X, Lu H, Li Z, Zhai Y, Ndione PF, et al. 2018. Impact of layer thickness on the charge carrier and spin coherence lifetime in two-dimensional layered perovskite single crystals. *ACS Energy Lett.* 3:2273–79
57. Zhou M, Sarmiento JS, Fei C, Zhang X, Wang H. 2020. Effect of composition on the spin relaxation of lead halide perovskites. *J. Phys. Chem. Lett.* 11:1502–7
58. Odenthal P, Talmadge W, Gundlach N, Wang R, Zhang C, et al. 2017. Spin-polarized exciton quantum beating in hybrid organic–inorganic perovskites. *Nat. Phys.* 13:894–99
59. Crane MJ, Jacoby LM, Cohen TA, Huang Y, Luscombe CK, Gamelin DR. 2020. Coherent spin precession and lifetime-limited spin dephasing in CsPbBr_3 perovskite nanocrystals. *Nano Lett.* 20:8626–33
60. Wang J, Zhang C, Liu H, McLaughlin R, Zhai Y, et al. 2019. Spin-optoelectronic devices based on hybrid organic–inorganic trihalide perovskites. *Nat. Commun.* 10:129
61. Pan R, Wang K, Yu Z-G. 2022. Magnetic-field manipulation of circularly polarized photoluminescence in chiral perovskites. *Mater. Horiz.* 9:740–47
62. Nestoklon MO, Goupalov SV, Dzhiyev RI, Ken OS, Korenev VL, et al. 2018. Optical orientation and alignment of excitons in ensembles of inorganic perovskite nanocrystals. *Phys. Rev. B* 97:235304
63. Xie Z, Markus TZ, Cohen SR, Vager Z, Gutierrez R, Naaman R. 2011. Spin specific electron conduction through DNA oligomers. *Nano Lett.* 11:4652–55
64. Lee H, Ma S, Oh S, Tan J, Lee CU, et al. 2023. Chirality-induced spin selectivity of chiral 2D perovskite enabling efficient spin-dependent oxygen evolution reaction. *Small* 19:2304166
65. Feng L-Z, Song Y-H, Li Z-D, Zhu B-S, Ma Z-Y, et al. 2024. Dimensional and doping engineering of chiral perovskites with enhanced spin selectivity for green emissive spin light-emitting diodes. *Nano Lett.* 24:6084–91
66. Zhang R, Tian Y, Ye C, Wang Y, Mi W, et al. 2024. Efficient quasi-2D perovskite spin light-emitting diodes based on chiral-induced spin selectivity. *Chem. Mater.* 36:3812–19
67. Wang J, Zhang C, Liu H, Liu X, Guo H, et al. 2019. Tunable spin characteristic properties in spin valve devices based on hybrid organic–inorganic perovskites. *Adv. Mater.* 31:e1904059
68. Abherve A, Mercier N, Kumar A, Das TK, Even J, et al. 2023. Chirality versus symmetry: electron’s spin selectivity in nonpolar chiral lead-bromide perovskites. *Adv. Mater.* 35:e2305784
69. Schmidt G, Ferrand D, Molenkamp LW, Filip AT, van Wees BJ. 2000. Fundamental obstacle for electrical spin injection from a ferromagnetic metal into a diffusive semiconductor. *Phys. Rev. B* 62:R4790–93
70. Liu T, Wang X, Wang H, Shi G, Gao F, et al. 2020. Linear and nonlinear two-terminal spin-valve effect from chirality-induced spin selectivity. *ACS Nano* 14:15983–91

68. mcp-AFM measurements on chiral halide perovskites, using a magnetic substrate instead of a magnetic tip.

71. Jonker BT, Park YD, Bennett BR, Cheong HD, Kioseoglou G, Petrou A. 2000. Robust electrical spin injection into a semiconductor heterostructure. *Phys. Rev. B* 62:8180–83
72. Ohno Y, Young DK, Beschoten B, Matsukura F, Ohno H, Awschalom DD. 1999. Electrical spin injection in a ferromagnetic semiconductor heterostructure. *Nature* 402:790–92
73. Zhu HJ, Ramsteiner M, Kostial H, Wassermeier M, Schönherr HP, Ploog KH. 2001. Room-temperature spin injection from Fe into GaAs. *Phys. Rev. Lett.* 87:016601
74. Etou K, Hiura S, Park S, Sakamoto K, Takayama J, et al. 2021. Room-temperature spin-transport properties in an $\text{In}_{0.5}\text{Ga}_{0.5}\text{As}$ quantum dot spin-polarized light-emitting diode. *Phys. Rev. Appl.* 16:014034
75. Hautzinger MP, Pan X, Hayden SC, Ye JY, Jiang Q, et al. 2024. Room-temperature spin injection across a chiral perovskite/III–V interface. *Nature* 631:307–12
76. Yao J, Wang Z, Huang Y, Xue J, Zhang D, et al. 2024. Efficient green spin light-emitting diodes enabled by ultrafast energy- and spin-funneling in chiral perovskites. *J. Am. Chem. Soc.* 146:14157–65
77. Jang G, Jo D-Y, Ma S, Lee J, Son J, et al. 2024. Core-shell perovskite quantum dots for highly selective room-temperature spin light-emitting diodes. *Adv. Mater.* 36:2309335
78. Yang C-H, Xiao H, Sang Y-F, Luo J, Xiao S-B, et al. 2024. In situ formed perovskite nanocrystal films toward efficient circularly polarized electroluminescence. *Adv. Funct. Mater.* 34:2310500
79. Ye C, Jiang J, Zou S, Mi W, Xiao Y. 2022. Core-shell three-dimensional perovskite nanocrystals with chiral-induced spin selectivity for room-temperature spin light-emitting diodes. *J. Am. Chem. Soc.* 144:9707–14
80. Yang C-H, Xiao S-B, Xiao H, Xu L-J, Chen Z-N. 2023. Efficient red-emissive circularly polarized electroluminescence enabled by quasi-2D perovskite with chiral spacer cation. *ACS Nano* 17:7830–36
- 81. Chen C, Gao L, Gao W, Ge C, Du X, et al. 2019. Circularly polarized light detection using chiral hybrid perovskite. *Nat. Commun.* 10:1927**
82. Wang J, Lu H, Pan X, Xu J, Liu H, et al. 2021. Spin-dependent photovoltaic and photogalvanic responses of optoelectronic devices based on chiral two-dimensional hybrid organic-inorganic perovskites. *ACS Nano* 15:588–95
83. Zhang X, Ye H, Liang L, Niu X, Wu J, Luo J. 2022. Direct detection of near-infrared circularly polarized light via precisely designed chiral perovskite heterostructures. *ACS Appl. Mater. Interfaces* 14:36781–88
84. Uchida K, Takahashi S, Harii K, Ieda J, Koshibae W, et al. 2008. Observation of the spin Seebeck effect. *Nature* 455:778–81
85. Zhang L, Niu Q. 2015. Chiral phonons at high-symmetry points in monolayer hexagonal lattices. *Phys. Rev. Lett.* 115:115502
86. Choi WJ, Yano K, Cha M, Colombari FM, Kim J-Y, et al. 2022. Chiral phonons in microcrystals and nanofibrils of biomolecules. *Nat. Photon.* 16:366–73
87. Zhu H, Yi J, Li M-Y, Xiao J, Zhang L, et al. 2018. Observation of chiral phonons. *Science* 359:579–82

81. First demonstration of using chiral halide perovskite for circularly polarized photodetector.
